Communications Earth & Environment https://doi.org/10.1038/s43247-025-03164-6

Article in Press

Shock demagnetization in an ambient magnetic field at the Dhala impact structure, India

Received: 10 June 2025

Accepted: 23 December 2025

Cite this article as: Pandey, A.K., Agarwal, A., Joshi, G. *et al.* Shock demagnetization in an ambient magnetic field at the Dhala impact structure, India. *Commun Earth Environ* (2026). https://doi.org/10.1038/s43247-025-03164-6

Ambrish Kumar Pandey, Amar Agarwal, Gaurav Joshi, Satish Sangode & Mamilla Venkateshwarlu

Shock demagnetization in an ambient magnetic field at the Dhala impact structure, India

Ambrish Kumar Pandey[1*], Amar Agarwal[1], Gaurav Joshi[1], Satish Sangode[2], Mamilla Venkateshwarlu[3]

[1]Applied Structural Geology Lab, Department of Earth Sciences, Indian Institute of Technology Kanpur, Kanpur, 208016, India.

[2]Department of Geology, Savitribai Phule Pune University, Pune, 411007, India.

[3]CSIR-National Geophysical Research Institute, Hyderabad, 500007, India.

*Corresponding author email: ambrish21@iitk.ac.in

Abstract

Impact-generated shock waves can modify the remanent magnetization preserved in target rocks, yet their effects remain poorly constrained. Here we examine how shock waves modify rock magnetisation by analysing unshocked granitoids and diorites, and shock-affected monomict breccia and impact melt rock of the Paleoproterozoic Dhala impact structure in India. Microscopic, thermomagnetic and hysteresis analyses were used to identify magnetic minerals and their domain states. Remanent magnetization and demagnetization experiments were performed to evaluate shock effects on the palaeomagnetic behaviour of impact-generated and unshocked target rocks. The unshocked rocks contain strong and stable magnetization carried by titanomagnetite. In contrast, the monomict breccia carries titanomagnetite and titanohematite and shows extremely weak and unstable magnetization, consistent with shock-related grain-size reduction and microfracturing. Impact melt rocks display intermediate behaviour, with titanomagnetite, titanohematite and pyrrhotite as magnetic carriers. These results show that shock can substantially reduce crustal magnetization, helping to explain weak magnetic signatures at terrestrial and planetary impact structures, even in the presence of an ambient magnetic field.

Introduction

Understanding the effects of impact-generated shock waves on the magnetic properties of the target lithology is essential for explaining the shock demagnetization and low magnetic intensities observed over many Martian craters and in shock-affected regions along the peripheries of major impact basins on Mars (e.g., Hellas, Argyre, and Isidis). Here, the low magnetic intensity may be attributed to several processes, including shock demagnetization [1,2], the non-acquisition of thermal remanent magnetization after dynamo cessation [3], excavation of crustal material that is more

strongly magnetized than the underlying mantle [4,5], or cooling in a reversing dynamo field [6,7]. According to the present state of knowledge, an impact can either demagnetize or remagnetize the target material and the impactites, depending on the absence or presence of an ambient magnetic field [1,5,8] generated by the dynamo operating within the planetary body. This argument has been used to place constraints on the timing of dynamo cessation on Mars [5,9–11].

Near the center of the Martian impact basins formed after dynamo cessation, both thermal and shock processes may have contributed to demagnetization. Contrary to the Martian setting, an ambient magnetic field on Earth may impart a stable thermal remanent magnetization (TRM) to the rocks near the crater center. TRM is acquired as these rocks cool down after being heated beyond the Curie temperature due to impact. For example, the Ries crater in Germany exhibits a negative magnetic anomaly at its center, which is attributed to the cooling of its ~400 m thick melt sheet during a period of reversed geomagnetic polarity. Similarly, the Manicouagan crater in Canada, with an impact melt sheet over 1 km thick, displays a positive central anomaly [12].

Notably, at the major Martian basins, shock demagnetization extends much farther, sometimes up to their periphery, thus affecting a larger volume of rocks [3,13]. These rocks experienced low shock temperatures, yet the mechanisms responsible for their demagnetization remain unclear. Similarly, monomict breccia, the most common impactite at the Dhala impact structure, experienced low shock temperatures. Even though the target granitoid rocks are ferrimagnetic [14], the structure features a low-intensity magnetic anomaly [15]. Thus, the cause of the low-intensity magnetic anomaly at the Dhala impact structure is critical to investigate. It will provide clues to understanding the shock demagnetization processes active at the periphery of the major Martian impact basins. Therefore, here we study the magnetic properties of the unshocked target rocks and impactites at the Dhala impact structure, India (see geological setting in Methods).

Our analyses show that shock modifies the ability of rocks to acquire and retain stable remanent magnetization, with the lowest remanence occurring in the shocked monomict breccias. In contrast, the impact melt rocks and unshocked lithologies preserve comparatively stable magnetic signals. These results demonstrate that shock processes alone can substantially reduce crustal magnetization in the presence of an ambient magnetic field. This provides a mechanism for subdued magnetic signatures in impact crater regions where thermal resetting is limited. This framework helps explain magnetic lows at terrestrial craters and offers new insight into how the

weak magnetic signatures characteristic of large Martian basins may arise from shock demagnetization in their peripheral zones, where thermal effects are minimal and an ambient magnetic field may still have been present.

Results

Outcrop and microscopic features

Impact melt rock forms six reddish-orange to pale brown-coloured outcrops around the CEA (Fig. 1, see geological setting in Methods). They present millimeter to centimeter size, circular to elliptical vesicles, some of which are filled by secondary minerals such as agate, quartz, and chlorite (Fig. 2a). The impact melt rocks exhibit an aphanitic to fine-grained texture and comprise predominantly lithic clasts, along with mineral and melt clasts. The primary mineral constituents include quartz, orthoclase, plagioclase feldspar, sericite, zircon, and opaque minerals. The shock metamorphic features, such as ballen-textured quartz and planar deformation features, are common (Fig. 3a, b). Titanomagnetite is the most common opaque phase, followed by titanohematite, observed in a few samples (Fig. 3c). There are two distinct types of magnetite: cubic, likely formed due to slower cooling in the target rocks and included in impact melt [16], and skeletal magnetite, indicative of rapid cooling and crystallization from impact melt.

At outcrop scale, the monomict breccia presents brecciated fragments of coarse to medium-grained granitoid clasts embedded within a finer clastic matrix (Fig. 2b). While at microscopic scale, large granitic clasts, primarily composed of quartz and feldspar, are surrounded by a fine-grained clastic matrix (Fig. 3d). Extensive fracturing is observed within the quartz clasts (Fig. 3e). Modal analysis indicates that the feldspar-to-quartz ratio in the clasts ranges between 60:30 and 40:50, with the remaining 10% consisting of accessory minerals such as chlorite, biotite, and various opaque minerals (Fig. 3e). Titanomagnetite is the dominant opaque phase, followed by Ti-hematite in a few monomict breccia samples (Supplementary Fig. 4).

The monomict breccia is surrounded by unshocked granitoid and diorite outcrops (Fig. 1), which exhibit minimal fracturing and brecciation (Figs. 2c, 2d). The granite is coarse-grained and equigranular, with visible feldspar, quartz, and biotite grains. At the microscale, unshocked granite consists of plagioclase clasts, quartz, and biotite, with sericite alteration derived from plagioclase and quartz (Fig. 3f). The diorite at the outcrop scale displays a medium to coarse-grained texture

with interlocking mineral grains (Fig. 2d), while at microscale they present predominantly hornblende, plagioclase, with minor amount of quartz (Fig. 3g).

Thermomagnetic behaviour

Unshocked granite (UG) and diorite (UD) exhibit high magnetization in their cooling curves, indicating phase transformations or mineral recrystallization during heating (Fig. 4a, b, and Supplementary Fig. 2 and Supplementary Table 3). The Curie transitions at T_{C1} (568 °C – 585 °C) represent Ti-poor magnetite in both rock types. The stoichiometric magnetite represented by T_{C1} remains stable throughout the experiment. The curves are irreversible with increased magnetization in the cooling curve at temperatures below T_{C1}. The increased magnetization may be due to the formation of a higher moment phase due to oxidation during heating of the sample [16]. The monomict breccia samples are also dominated by Ti-magnetite, with occasional occurrences of Ti-hematite (Supplementary Figs. 4 and 3g,h) [14].

The impact melt rock presents up to three distinct Curie transitions, T_{C2}, T_{C3}, and T_{C4} (Fig. 4c, d, Supplementary Fig. 3 and Supplementary Table 3). T_{C2}, 518 °C – 545 °C, is attributed to Ti-magnetite, but with higher titanium content (ulvöspinel 0.05-0.10) than in unshocked granite and diorite [17]. T_{C3} (321 °C – 351 °C) represents pyrrhotite [18,19]. While, T_{C4}, 617 °C – 633 °C, characteristic of Ti-hematite [20] is observed only in I3.12 and I6.18 (Fig. 4d and Supplementary Fig. 3f). Curves of all impact melt rock samples have comparable shapes and are reversible, indicating the stability of the three magnetic carriers during heating in air (Fig. 4c, d; Supplementary Fig. 3).

Bulk domain state

The hysteresis curves of unshocked granite and diorite are narrow (Fig. 5a,b and Supplementary Fig. 1), typical of MD magnetic grains [21]. In contrast, impact melts exhibit wasp-waisted hysteresis curves, indicating low-coercivity ferromagnetic grains such as SD or PSD magnetite with SP fractions (Fig. 5c,d and Supplementary Fig. 1) [19,22,23]. Monomict breccia shows pot-bellied and wasp-waisted hysteresis loops [14]. Remanence of coercivity (H_{cr}) is lower in unshocked granite (8.53–21.45 mT) and diorite (7.41–23.31 mT), compared to impact melt rock (39.32–109.92 mT) and monomict breccia (27.54–49.38 mT), revealing increased single-domain (SD) content (Fig. 5, Supplementary Table 2). Bulk coercivity (H_c) trends are in agreement, with lower values in unshocked granite and diorite, and higher values in impact melt rock and monomict breccia.

The Day-Dunlop plot (Fig. 5e) reveals that the MD component is highest in the unshocked rocks, > 85%, followed by the impact melt rock, 60 to 40%, and monomict breccia, 60 to 0 %. The impact melt rocks plot in the PSD field, which likely reflects averaging of multiple magnetic populations, e.g., inherited titanomagnetite, fine-grained magnetite, and pyrrhotite. The monomict breccia and the unshocked rocks plot along the SD–MD mixing line, with more than 40% SD component (Fig. 5e). Although dominated by MD-like behavior, the hysteresis parameters of the unshocked rocks are also consistent with prolate vortex states [24].

Susceptibility and remanent magnetization

Unshocked rocks present the lowest values of frequency-dependent susceptibility, $0.29\% \geq \chi_{fd}\% \geq 1.06\%$, preceded by monomict breccia ($7.26\% \geq \chi_{fd}\% \geq 8.82\%$); while the values are highest, $2.01\% \geq \chi_{fd}\% \geq 47.55\%$, in impact melt rocks (Supplementary Table 4). Low χ_{fd} value in unshocked rocks is owed to MD grains, which is in agreement with the hysteresis results. In contrast, high χ_{fd} values in impact melt rocks exceed the 15% threshold typical of SP behavior [25,26], and in some cases, reach the range reported for extremely fine magnetic particles [27,28]. This is coherent with the wasp-waisted hysteresis of the impact melt rocks [23].

Unshocked granite and diorite have comparable bulk magnetic susceptibility (χ), ranging from 0.24×10^{-3} to 1.49×10^{-3} SI (Supplementary Table 1). The monomict breccia presents the lowest, $0.13 \times 10^{-3} \geq \chi \geq 0.34 \times 10^{-3}$ SI. The impact melt rocks have the highest susceptibility, $0.66 \times 10^{-3} \geq \chi \geq 1.86 \times 10^{-3}$ SI.

NRM intensities in the unshocked granite and unshocked diorite are comparable. The former ranges from 1.61 to 10.52 A/m and the latter from 1.50 to 10.37 A/m (Fig. 6, Supplementary Table 1). In contrast, the NRM intensity of the monomict breccia is generally two orders of magnitude lower, 5.0×10^{-3} to 1.7×10^{-2} A/m (avg. = 9.0×10^{-3} A/m). NRM intensities in impact melt rocks fall in between the unshocked rocks and monomict breccia, ranging from 3.0×10^{-2} A/m to 6.5×10^{-1} A/m (avg. = 2.2×10^{-1} A/m).

Unshocked rocks have much higher Koenigsberger (Q) ratios than the impactites. The unshocked granite and diorite have a high (Q) ratio, 118.2 to 702.3 (Fig. 6, Supplementary Table 1), indicating that magnetization is largely controlled by remanence. Among the impactites, the impact melt rocks have slightly higher Q ratios, 1.3 to 14.6, than the monomict breccia, 0.35 to 1.50. In the

impactites the magnetization, in some cases, is controlled by induced magnetization ($Q < 1$), and in other cases, $1 \leq Q < 10$, by a combination of remanent and induced magnetization [18,29]. Two unshocked samples (UG3, UG7) with anomalously high Q ratios (1310.0 and 875.3), unusually strong NRM intensities (44.6 and 88.1 A/m, nearly an order of magnitude greater than other unshocked specimens), and unstable demagnetization behaviour were excluded, consistent with lightning strike overprints (see "discarded" in Supplementary Table 1) [30,31].

Consistent with these trends, the mass-normalized isothermal remanent magnetization (IRM) and anhysteretic remanent magnetization (ARM) intensities exhibit systematic lithology-dependent variations (Supplementary Fig. 5). Average values of $SIRM_{1000mT}$ (saturation isothermal remanent magnetization) and ARM decrease from unshocked rocks (6.7×10^{-1} and 1.03×10^{-2} Am^2 kg^{-1}) to impact melts (1.11×10^{-2} and 3.65×10^{-5} Am^2 kg^{-1}) and monomict breccia (4.18×10^{-3} and 2.18×10^{-6} Am^2 kg^{-1}), respectively. These results indicate a progressive reduction in remanence acquisition capacity from unshocked rocks to monomict breccia, with unshocked lithologies exhibiting the highest ARM/SIRM ratios, impact melts showing intermediate ratios, and monomict breccia the lowest.

Alternating Field and Thermal Demagnetization Results

Unshocked granite and diorite show a low-coercivity antiparallel component that is removed by 10 mT during AF demagnetization (Fig. 7a-d; Supplementary Fig. 6; Supplementary Table 5). This secondary component is present in most unshocked samples and is interpreted as a low-coercivity secondary overprint rather than a viscous remanent magnetization (VRM), as its direction deviates from the present geomagnetic field. Further demagnetization isolates an intermediate-coercivity, stable component whose magnetization intensity decays gradually (red symbols in Fig. 7a–d). Of the eight unshocked sites, three yielded moderately clustered and distinct ChRMs (Fig. 8; Supplementary Fig. 6; Supplementary Table 5), while the remaining sites did not provide stable directions. By contrast, monomict breccia shows unstable behavior during both AF and thermal demagnetization, with no consistent ChRM isolated across specimens (Fig. 7e-h; Supplementary Fig. 7).

Most impact melt rock samples display a stable component during both alternating-field (AF) and thermal demagnetization, without any secondary overprint (Fig. 7i-l; Supplementary Fig. 8;

Supplementary Table 6). Orthogonal plots show linear decay trajectories toward the origin, while stereoplots illustrate vector clustering. A few specimens (e.g., 10.1, 11.1, 13.1) exhibit a weak secondary overprint that is not VRM. After removal of this component, further demagnetization isolates a stable component, similar to that in the samples lacking the secondary overprint. The mean ChRM direction of the impact melt rock has a declination of 169°, an inclination of 38.2°, with a Fisher precision parameter k = 9.8 and an α_{95} of 9.3° (Fig. 8; Supplementary Fig. 8; Supplementary Table 6). The modest scatter in the ChRM directions of individual melt rock specimens likely reflects magnetic heterogeneity within the melt arising from variations in mineralogy and domain state (Fig. 8).

Discussion

To understand the effects of hypervelocity impact-generated shock waves on the magnetization, we compare the magnetic properties of the unshocked target rocks with the monomict breccia and the impact melt rocks. Our results reveal that in the unshocked rocks, MD grains of low-Ti magnetite carry magnetic signals and lead to intermediate magnetic susceptibility, high NRM intensity, and stable paleomagnetic directions (Figs. 6, 7a-d, 8, Supplementary Fig. 6).

The impact melt rocks feature the highest magnetic susceptibility, intermediate NRM intensities, and stable paleomagnetic directions (Figs. 6, 7i-l, Supplementary Fig. 8). Joshi et al. [32] suggested that at least some of the Ti-magnetite grains in the impact melt rocks are derived from the target rocks. Similar to the Ti-magnetite in the monomict breccia, they would also have experienced shock waves that caused domain defects and domain size reduction [33,34]. However, the high temperatures within the impact melt would have annealed any shock effects [35,36], and these magnetic grains subsequently acquired thermal remanent magnetization during cooling, along with other PSD grains that crystallized as the impact melt solidified.

Our frequency-dependent susceptibility measurements reveal SP particles in impact melt rocks. The rapid cooling, which produced the skeletal grains [32], could have formed these SP particles. The MCB-10 borehole [37] revealed ~70 m thick impact melt rock deposits, which most probably cooled within years at the margins, but took centuries near the center. This estimate is based on comparison with cooling times of the ~200 m thick Ries melt sheet [38]. The SP particles impart high susceptibility values to the impact melt rocks. The dominance of SP over PSD particles explains the intermediate Q-ratios and NRM intensity (Fig. 6). SP grains contribute to magnetic

susceptibility, but do not sustain long-term remanence [23]. Stable remanence in impact melt rocks is carried by PSD grains [39].

The coercivity of remanence (H_{cr}) and bulk coercivity (H_c) are higher in impactites compared to unshocked rocks. In impact melt rocks, this increase in coercivity can be attributed to the formation of high coercivity phases such as pyrrhotite and occasional hematite. Pyrrhotite may have formed due to hydrothermal activity during the early stages of cooling of impact melt rocks. It enhances coercivity while contributing little to remanence. Instead, the persistence of stable directions at high unblocking temperatures and high coercivities shows that Ti-magnetite carries the ChRM (Fig. 7i–l, Supplementary Fig. 8). Titanohematite occurs occasionally along Ti-magnetite grain margins in both impact melt and monomict breccia and is absent in the unshocked target rocks. Its occurrence is best explained by localized oxidation of Fe–Ti oxides, consistent with reports from other impact melt sheets [40]. The monomict breccia presents magnetic properties that contrast with those of the unshocked and impact melt rocks, showing lower magnetic susceptibility, extremely low NRM intensities, and unstable paleomagnetic directions (Figs. 6, 7e-h, Supplementary Fig. 7). The cause of these differences lies in the formation of the monomict breccia, which is detailed below.

Previous studies suggest that the shock waves fractured and brecciated the target granites to form monomict breccia [14,41]. During brecciation, the MD Ti-magnetite in unshocked granite developed fractures and domain defects, leading to a decrease in apparent domain size and an increase in coercivity [35]. Shock-induced defects suppress the ability of grains to carry remanence, leading to lower NRM and susceptibility relative to the unshocked rocks. In agreement with this, other studies on naturally and experimentally shocked rocks suggest that microfracturing and domain wall pinning induced by shock can cause MD grains to mimic SD-like behavior [2,8,36,42,43]. In general, SD grains are paleomagnetically more stable than MD grains [44]. Thus, the SD-like behavior of the Ti-magnetite in monomict breccia does not explain unstable paleomagnetic directions.

Large-scale randomization due to mixing in monomict breccia is precluded because Tiwari et al. [14] showed that the monomict breccia samples collected 10-20 meters apart present well-developed magnetic fabric and comparable orientation. They concluded that the monomict breccia experienced no displacement or mixing. However, at the millimeter scale, individual clasts in the monomict breccia are randomly oriented (Fig. 2d). This small-scale physical randomization is

sufficient to partially cancel the magnetic vectors of ~10 cm³ specimens, and lead to the low NRM and unstable paleomagnetic directions in monomict breccia.

Experimental studies have revealed loss of NRM due to low shock pressures of ~2 GPa and under hydrostatic compression of ~1.24 GPa [2,8,45–50]. Shock demagnetization mechanisms differ in different domain states. In MD grains, compressive stresses decrease the total volume of domains with spontaneous magnetization aligned parallel to the compression axis [48,51]. This irreversible domain realignment results in a measurable reduction in the NRM intensity and susceptibility. In SD grains, the shock wave strains the domains, increasing the magnetostrictive energy beyond the magnetocrystalline anisotropy, thereby reducing the remanent magnetization and susceptibility [1,52–54].

In summary, the low NRM and unstable paleomagnetic directions in the monomict breccia likely result from a combination of millimeter-scale clast randomization, which reduces net remanent magnetization, and shock-induced domain-level modifications, where fractures and domain defects in MD Ti-magnetite weaken remanence despite SD-like hysteresis behaviour.

Several lines of evidence argue against hydrothermal alteration as the cause of demagnetization in the monomict breccia. First, in monomict breccia, ARM and IRM data show very low remanence efficiency (Supplementary Fig. 5), with SIRM intensities and ARM/SIRM ratios consistently an order of magnitude lower than in impact melts and unshocked lithologies. Thus, monomict breccia is unable to acquire remanence. Second, Ti-magnetite is the primary magnetic carrier in monomict breccia, and is occasionally altered to Ti-hematite along its grain boundaries (Supplementary Fig. 4) [14]. Third, the Giant Quartz Veins at Dhala represent three phases of regional hydrothermal activity [55], that affected both unshocked lithologies and impactites. Hydrothermal activity generally produces low-intensity stable chemical remanent magnetization [40,56,57]. These stable directions are distinct for each site, and ChRM directions in samples collected over a larger hydrothermally altered area do not present comparable directions. However, the monomict breccia features unstable directions.

Thus, the absence of stable directions in monomict breccia, together with only minor alterations in Ti-magnetite, indicates that hydrothermal activity did not substantially affect the magnetic mineralogy and paleomagnetic characteristics.

Further supporting evidence comes from the impact melt rocks. Here, Ti-magnetite grains are altered to Ti-hematite along the margins (Fig. 3c), and some samples (I1, I2.8, I3.13 and I3.31) contain hydrothermal pyrrhotite (Fig. 3c, d, Supplementary Fig. 3). Despite these secondary phases, most samples yield stable ChRM directions that are comparable throughout the six impact melt outcrops. Thus, as with the monomict breccia, hydrothermal alteration did not affect the remanent magnetization of the impact melt rocks.

Our current understanding suggests that impact cratering and shock waves can remagnetize and demagnetize rocks depending on the presence or absence of an ambient field. Impact melt rocks record the ambient field during impact and control magnetic anomalies. For example, Manicouagan and Ries impact structures are characterized by thick coherent melt sheets that dominate their paleomagnetic signals, producing magnetic anomalies consistent with the geomagnetic polarity at the time of impact, positive over Manicouagan, negative over Ries [12,58].

Impact cratering may generate a plasma field that momentarily shields the impactites from the ambient field, leading to demagnetization [59]; however, this explanation remains speculative at this stage, as plasmas have also been shown to amplify magnetic fields [60,61]. At older or smaller terrestrial craters, impact melt sheets are often not preserved. The scaling laws predict that even small simple craters can generate melt layers [62] and impact melt has been observed in lunar craters as small as 170 m in diameter [63]. However, the preservation potential of impact melt at small terrestrial craters is much lower due to erosion and limited melt volumes. Thus, the magnetic anomalies may be controlled by shocked target rocks. One such example is the Santa Fe impact structure in the USA (crater diameter 6–13 km), where shock demagnetization has been attributed to plasma shielding of the ambient field [59]. This led to the momentary absence of the ambient field when the rocks were shocked, as proposed by the authors.

In the case of impact craters on Mars, which formed after the cessation of the dynamo, the melt rocks cool down in the absence of an ambient field, leading to low magnetic anomalies. However, weak magnetization at Martian craters can also arise through several processes that operate even when a dynamo generated magnetic field is present. Low magnetic anomalies at Martian impact basins have been explained by several processes, including excavation of strongly magnetized crust that exposes deeper, weakly magnetized material [4,5] and cooling through a reversing dynamo, which can produce subdued anomalies despite an active field [6,7]. Shock demagnetization has also

been invoked to explain magnetic lows at both Martian basins [2] and terrestrial structures such as Santa Fe [59].

Our results provide an additional perspective on these interpretations. They show that weak magnetization can also arise in peripherally shocked regions, even when an ambient magnetic field is present, a process that complements previously proposed mechanisms focused mainly on melt-sheet behavior near the centers of large basins. Our findings, therefore, help constrain how magnetization may be reduced outside the melt sheet, particularly in the peripheral regions where shock effects dominate, and thermal annealing is limited.

The principal magnetic carriers on Mars are magnetite, hematite, and pyrrhotite, which occur in a range of domain states [64,65] and are also present at Dhala. The Dhala structure is ~11 km in diameter, smaller than Martian impact basins that can be magnetically characterized from orbital data, with the largest examples such as Hellas, Argyre, and Isidis exceeding 1000 km in diameter. In large basins, the crust is interpreted to be completely demagnetized within ~0.8 crater radii by a combination of thermal and shock effects, while beyond the rim (>1.4 radii), shock effects dominate, producing partial demagnetization [13]. Interior basin temperatures would have been far higher than those of the Dhala impact melt, likely melting and annealing shock-modified grains. Our results are, therefore, most relevant to the peripheral zones of larger basins, where shock-induced changes to domain structure and clast-scale randomization could survive the relatively lower shock temperatures. These results may also be relevant for smaller Martian impact structures whose magnetic signatures are not yet resolved from existing orbital satellite data [5].

Conclusions

This study investigated the rock magnetic properties of unshocked target rocks, monomict breccia, and impact melt rocks at the Dhala Impact structure. The unshocked lithologies present the highest values of NRM and Q-ratio, and intermediate magnetic susceptibility. Impact melt rocks present intermediate values of NRM and Q-ratio and stable paleomagnetic vectors. They feature the highest magnetic susceptibility. Such magnetic behaviour is attributed to PSD and SP grains. Some PSD grains were inherited from the pre-impact target lithologies, while the SP particles crystallized during rapid cooling of the impact melt.

The monomict breccia exhibits much lower values of NRM and Q-ratio and unstable paleomagnetic vectors. Shock caused micro-fracturing and domain defects in magnetic minerals, producing SD-like hysteresis behaviour in originally MD grains but weakening their ability to carry remanence. Clast-scale randomization leads to cancellation of magnetic vectors at the specimen scale. Together, these processes rendered the low NRM intensity and unstable directions and produced the apparent shock demagnetization of the monomict breccia. Thus, the subdued magnetic signatures at impact structures cannot be attributed to a single process or the absence of an ambient field. Shock demagnetization may have contributed to the weak magnetization observed in the peripheral regions of large basins and in smaller impact craters on Earth and other planetary bodies. This study demonstrates that shock may demagnetize rocks even in the presence of an ambient magnetic field.

Methods

Geological Setting

The Dhala impact structure (Fig. 1), located in the Shivpuri district of Madhya Pradesh, India, is a Paleoproterozoic impact crater, 1.7-2.5 billion years old, with an original diameter of about 11 km [66]. The eroded remnant of the structure has a present-day diameter of ~ 4.5 km [14]. The target lithologies at the Dhala structure are part of the Archean crystalline basement of the Bundelkhand craton, which comprises older tonalite-trondhjemite-granodiorite (TTG) gneisses (2.7-3.6 Ga), intruded by diorites and granites of ~2.5 Ga [67]. Two to three phases of hydrothermal activity between ~ 1.4 and 2.0 Ga formed the giant quartz veins along the preexisting fractures [55]. This was followed by the intrusion of tholeiitic dykes ~ 1.1 to 2 Ga [68]. Three major deformation phases have affected the area, the first two resulting from compressive tectonic regimes which led to the folding of TTG gneisses (~3.7-2.7 Ga), and the third deformation occurred during granitic intrusion from 2.56 to 2.44 Ga [69].

The stratigraphy of the impactites at the Dhala structure is based on Mohar Cauldron Borehole drill data and outcrop exposures [37]. The impactite lithologies include pseudotachylitic breccias, monomict breccia, impact melt rocks, and suevites. Monomict breccia and impact melt rocks are exposed and studied here, while suevite and pseudotachylite breccia are recorded in borehole [37]. Among the two, monomict breccia is far more extensively and frequently exposed, with more than 200 outcrops forming a ring-like pattern that defines the outermost limit of the present-day crater

rim [14]. Many of the reddish-brown monomict breccia outcrops show a low, rounded, and elongated morphology with convex profiles [70]. Monomict breccia is suggested to have formed in situ due to the fracturing and brecciation of the target granite [14].

Six outcrops of impact melt rock are exposed at Dhala, all in the northern and western parts of the structure, likely due to the erosion of the rest. In the excavation stage, the impact melt flowed eastward in a semi-molten, lava-like state and was subsequently emplaced within the crater as crater-fill impactites [32]. The impact melt remained semi-molten, with temperature below ~1500 °C, with some pre-impact Ti-poor magnetite grains still present [32].

The post-impact lithologies feature Dhala formation and Sumen sandstone, equivalent to the Semri and Kaimur groups of the Vindhyan Supergroup, respectively. The Dhala Formation is primarily composed of sandstone, siltstone, shales, and conglomerates, with the dominant minerals being poorly sorted angular quartz clasts, feldspar, biotite, and sericite. Sumen Sandstone is partially covered by a laterized conglomerate at the top [71]. These sediments are exposed at a geomorphic mesa-like structure, called the Central Elevated Area (CEA). The CEA is ~ 418 meters above mean sea level, covering an area of ~ 5 km^2.

Sampling and Palaeomagnetic Analyses

To analyze the microscopic and magnetic properties of the impact melt rocks, monomict breccia, and unshocked target rock, samples were collected during two field campaigns. Fractured and weathered outcrops were avoided. For impact melt rocks, 34 oriented cylindrical cores were drilled, each measuring 1 inch in diameter and 4-5 inches in length, from 6 paleomagnetic sites (Fig. 1) using a portable hand drill. The cylinders were oriented using a magnetic compass before being removed from the impact melt rocks. Oriented block samples of monomict breccia and unshocked target rock were collected from 4 and 8 paleomagnetic sites, respectively. The blocks were drilled in the lab to retrieve cylinders, which were then cut into specimens, 2.54 cm in diameter and 2.2 cm in length. Unshocked target rocks do not exhibit extensive fracturing, brecciated clasts, or vesicles, making them easily distinguishable from impactites in the field. Larger outcrops have more than one sampling site to average out local variations (Supplementary Table 1).

The temperature-dependent magnetization (M-T) analysis was conducted using an Advanced Variable Field Translation Balance at the Paleomagnetism Laboratory, CSIR–NGRI, Hyderabad, having a sensitivity of 5×10^{-5} Am^2. This technique measures the magnetic dipole moment (M) as a function of temperature (T), either in a zero field or an applied field. M-T curves are used to determine the Curie temperature (Tc) using the 1st derivative method [72] to know the stability of the principal magnetic carriers and the phase changes during heating and cooling (Supplementary Table 3).

Hysteresis loops were obtained using a Vibrating Sample Magnetometer (Model EV7-VSM; ADE Technologies, USA) with a sensitivity of ~ 1×10^{-9} Am^2, under a maximum applied field of 1.75 T at the Advanced Centre for Material Science, IIT Kanpur. Paramagnetic correction was performed by subtracting the linear portion of the hysteresis loop, observed after the ferromagnetic component saturates [19]. The correction interval varied depending on lithology: for impact melt rocks, it was applied above ~ 1124 mT, and for unshocked rocks above ~ 640 mT. HystLab software, version 1.1.2 [73], was used to calculate the coercive force (H_c), remanent magnetization (M_{rs}), and saturation magnetization (M_s). The remanence of coercivity (H_{cr}) was determined using the curve-shifting method [19]. The ratios H_{cr}/H_c and M_{rs}/M_s were plotted on the Day plot [74,75] to estimate the relative proportions of single domain (SD), multi-domain (MD), and pseudo-single domain (PSD) (Supplementary Table 2).

High-frequency (χ_{hf}, 4.6 kHz) and low-frequency (χ_{lf}, 0.46 kHz) magnetic susceptibility of selected samples of unshocked rocks and impactites were measured to determine frequency-dependent susceptibility (χ_{fd}%) using a dual-frequency MS2B Sensor (Bartington Instruments Ltd.) with a sensitivity of 1×10^{-6} SI (Supplementary Table 4). χ_{fd} % was calculated using the equation:

$$\chi_{fd}\% = [(\chi_{lf} - \chi_{hf}) / \chi_{lf}] \times 100$$

Bulk magnetic susceptibility (χ) of unshocked target rock was measured using a Kappabridge MFK-1A, which has a sensitivity of 2×10^{-8} SI at the Paleomagnetism Laboratory, CSIR–NGRI, Hyderabad, while χ data for impact melt rock and monomict breccia have been taken from earlier published reports (Supplementary Table 1) [14,32].

Natural remanent magnetization (NRM) was measured using a spinner magnetometer (Mu-Spin, Kodama Scientific Instruments, Japan) with a sensitivity of 10^{-11} Am^2 before demagnetization. A

subset of impact melt specimens (n = 11), monomict breccia (n = 5), and unshocked target rocks (n = 8) were used for isothermal remanent magnetization (IRM) and anhysteretic remanent magnetization (ARM) analyses. IRM was induced with an ASC Scientific Impulse Magnetizer (IM-10-30, USA) in stepwise fields up to 1000 mT (increments of 10–200 mT) at room temperature, and ARM was induced with a Magnon AFD 300 alternating-field demagnetizer using a 100 mT peak alternating field and a 100 μT DC bias. The resulting IRM and ARM were measured with the same Mu-Spin magnetometer.

Specimens from impact melt (n = 23), monomict breccia (n = 5), and unshocked target rocks (n = 15) were subjected to alternating-field demagnetization (AFD) using a three-axis AGICO LDA 3A demagnetizer (AGICO, Czech Republic) in eight steps up to 100 mT. Thermal demagnetization was carried out on representative specimens of impact melt (n = 4) and monomict breccia (n = 5) with an MMTD 80A thermal demagnetizer (Magnetic Measurements Ltd., UK) in 14 steps from 100-700 °C. Natural remanent magnetization (NRM), isothermal remanent magnetization (IRM), anhysteretic remanent magnetization (ARM), alternating field demagnetization (AFD), and thermal demagnetization (TD) and dual frequency magnetic susceptibility measurement were conducted at the Rock Magnetic Laboratory, Department of Geology, Savitribai Phule Pune University (SPPU), Pune. Zijderveld diagrams were generated in PuffinPlot (v1.4.1) [76], which was also used for principal component analysis (PCA) to determine characteristic remanent magnetization (ChRM) directions, and for calculating Fisher statistics, k (a measure of the concentration of directions about the mean direction) and α_{95} (the 95% confidence cone), for site-mean directions assuming a Fisher distribution [77].

The Koenigsberger (Q) ratio, defined as the ratio of remanent magnetization to induced magnetization [78], was calculated using the formula:

$$Q = NRM / (\chi \times 37.56\ A/m)$$

where 37.56 A/m represents the present-day geomagnetic field intensity at the Dhala structure.

Data availability

All data analyzed in this study, including raw paleomagnetic measurements, thermomagnetic data, hysteresis data, and all datasets used to produce the figures and tables in the main manuscript and

Supplementary Information, have been deposited in Figshare and are publicly available at [79]: https://doi.org/10.6084/m9.figshare.30851126

6. References

1. Louzada, K. L., Stewart, S. T., Weiss, B. P., Gattacceca, J. & Bezaeva, N. S. Shock and static pressure demagnetization of pyrrhotite and implications for the Martian crust. *Earth Planet. Sci. Lett.* **290**, 90–101 (2010).

2. Louzada, K. L. *et al.* Impact demagnetization of the Martian crust: Current knowledge and future directions. *Earth Planet. Sci. Lett.* **305**, 257–269 (2011).

3. Lillis, R. J., Stewart, S. T. & Manga, M. Demagnetization by basin-forming impacts on early Mars: Contributions from shock, heat, and excavation. *J. Geophys. Res. Planets* **118**, 1045–1062 (2013).

4. Mittelholz, A., Johnson, C. L., Feinberg, J. M., Langlais, B. & Phillips, R. J. Timing of the martian dynamo: New constraints for a core field 4.5 and 3.7 Ga ago. *Sci. Adv.* **6**, 1–7 (2020).

5. Mittelholz, A. *et al.* Magnetic Field Signatures of Craters on Mars. *Geophys. Res. Lett.* **51**, 1–10 (2024).

6. Rochette, P. Crustal magnetization of Mars controlled by lithology or cooling rate in a reversing dynamo? *Geophys. Res. Lett.* **33**, 2006–2009 (2006).

7. Steele, S. C. *et al.* Weak magnetism of Martian impact basins may reflect cooling in a reversing dynamo. *Nat. Commun.* **15**, 6831 (2024).

8. Gattacceca, J. *et al.* Unraveling the simultaneous shock magnetization and demagnetization of rocks. *Phys. Earth Planet. Inter.* **182**, 42–49 (2010).

9. Lillis, R. J., Robbins, S., Manga, M., Halekas, J. S. & Frey, H. V. Time history of the Martian dynamo from crater magnetic field analysis. *J. Geophys. Res. Planets* **118**, 1488–1511 (2013).

10. Vervelidou, F., Lesur, V., Grott, M., Morschhauser, A. & Lillis, R. J. Constraining the Date of the Martian Dynamo Shutdown by Means of Crater Magnetization Signatures. *J. Geophys. Res. Planets* **122**, 2294–2311 (2017).

11. Arkani-Hamed, J. Timing of the Martian core dynamo. *J. Geophys. Res. Planets* **109**, E03006 (2004).

12. Gilder, S. A., Pohl, J. & Eitel, M. Magnetic Signatures of Terrestrial Meteorite Impact Craters: A Summary. in *Magnetic Fields in the Solar System* (eds. Lühr, H., Wicht, J., Gilder, S. A. & Holschneider, M.) vol. 448 357–382 (Springer International Publishing, Cham, 2018).

13. Mohit, P. S. & Arkani-Hamed, J. Impact demagnetization of the martian crust. *Icarus* **168**, 305–317 (2004).

14. Tiwari, S., Joshi, G., Phukon, P., Agarwal, A. & Venkateshwarlu, M. Emplacement of monomict breccia and crater size estimate at the Dhala impact structure, India. *Meteorit. Planet. Sci.* **60**, 663–679 (2025).

15. Markandeyulu, A. *et al.* Application of high resolution airborne geophysical data in geological modelling of Mohar Cauldron Complex, Bundelkhand Massif, central India: implications for uranium exploration. *Explor. Geophys.* **45**, 134–146 (2014).

16. Alva-Valdivia, L. M., Rodríguez-Trejo, A., Morales, J., González-Rangel, J. A. & Agarwal, A. Paleomagnetism and age constraints of historical lava flows from the El Jorullo volcano, Michoacán, Mexico. *J. South Am. Earth Sci.* **93**, 439–448 (2019).

17. Lattard, D., Engelmann, R., Kontny, A. & Sauerzapf, U. Curie temperatures of synthetic titanomagnetites in the Fe-Ti-O system: Effects of composition, crystal chemistry, and thermomagnetic methods. *J. Geophys. Res.* **111**, B12S28 (2006).

18. Direen, N. G., Pfeiffer, K. M. & Schmidt, P. W. Strong remanent magnetization in pyrrhotite: A structurally controlled example from the Paleoproterozoic Tanami orogenic gold province, northern Australia. *Precambrian Res.* **165**, 96–106 (2008).

19. Tauxe, L. *Paleomagnetic Principles and Practice*. vol. 17 (2003).

20. Alva-Valdivia, L. M. *et al.* Nature inspired synthesis of magnetite nanoparticle aggregates from natural berthierine. *RSC Adv.* **13**, 32054–32062 (2023).

21. Alva-Valdivia, L. M., Guerrero-Díaz, P., Urrutia-Fucugauchi, J., Agarwal, A. & Caballero-Miranda, C. I. Review of magmatic iron-ore mineralization in central-western Mexico: Rock-magnetism and magnetic anomaly modelling of Las Truchas, case study. *J. South Am. Earth Sci.* **97**, 102409 (2020).

22. Alva-Valdivia, L. M. *et al.* Paleomagnetism and tectonics from the late Pliocene to late Pleistocene in the Xalapa monogenetic volcanic field, Veracruz, Mexico. *GSA Bull.* **131**, 1581–1590 (2019).

23. Fabian, K. Some additional parameters to estimate domain state from isothermal magnetization measurements. *Earth Planet. Sci. Lett.* **213**, 337–345 (2003).

24. Williams, W. *et al.* Vortex Magnetic Domain State Behavior in the Day Plot. *Geochemistry, Geophys. Geosystems* **25**, (2024).

25. Dearing, J. A. *et al.* Frequency-dependent susceptibility measurements of environmental materials. *Geophys. J. Int.* **124**, 228–240 (1996).

26. Peters, C. & Dekkers, M. J. Selected room temperature magnetic parameters as a function of mineralogy, concentration and grain size. *Phys. Chem. Earth, Parts A/B/C* **28**, 659–667 (2003).

27. Muxworthy, A. R. Effect of grain interactions on the frequency dependence of magnetic susceptibility. *Geophys. J. Int.* **144**, 441–447 (2001).

28. Worm, H. & Jackson, M. The superparamagnetism of Yucca Mountain Tuff. *J. Geophys. Res. Solid Earth* **104**, 25415–25425 (1999).

29. Clark, D. A. Magnetic petrophysics and magnetic petrology: aids to geological interpretation of magnetic surveys. *AGSO J. Aust. Geol. Geophys.* **17**, 83–103 (1997).

30. Salminen, J., Pesonen, L. J., Reimold, W. U., Donadini, F. & Gibson, R. L. Paleomagnetic and rock magnetic study of the Vredefort impact structure and the Johannesburg Dome, Kaapvaal Craton, South Africa-Implications for the apparent polar wander path of the Kaapvaal Craton during the Mesoproterozoic. *Precambrian Res.* **168**, 167–184 (2009).

31. Carporzen, L., Weiss, B. P., Gilder, S. A., Pommier, A. & Hart, R. J. Lightning remagnetization of the Vredefort impact crater: No evidence for impact-generated magnetic fields. *J. Geophys. Res. Planets* **117**, 1–17 (2012).

32. Joshi, G., Phukon, P., Agarwal, A. & Ojha, A. K. On the Emplacement of the Impact Melt at the Dhala Impact Structure, India. *J. Geophys. Res. Planets* **128**, e2023JE007840 (2023).

33. Agarwal, A. & Alva-Valdivia, L. M. Curie temperature of weakly shocked target basalts at the Lonar impact crater, India. *Earth, Planets Sp.* **71**, 141 (2019).

34. Agarwal, A., Kontny, A., Kenkmann, T. & Poelchau, M. H. Variation in Magnetic Fabrics at Low Shock Pressure Due to Experimental Impact Cratering. *J. Geophys. Res. Solid Earth* **124**, 9095–9108 (2019).

35. Reznik, B., Kontny, A., Fritz, J. & Gerhards, U. Shock-induced deformation phenomena in magnetite and their consequences on magnetic properties. *Geochemistry, Geophys. Geosystems* **17**, 2374–2393 (2016).

36. Reznik, B., Kontny, A. & Fritz, J. Effect of moderate shock waves on magnetic susceptibility and microstructure of a magnetite-bearing ore. *Meteorit. Planet. Sci.* **52**, 1495–1504 (2017).

37. Pati *et al.* Pseudotachylitic breccia from the Dhala impact structure, north-central India: Texture, mineralogy and geochemical characterization. *Tectonophysics* **649**, 18–32 (2015).

38. Onorato, P. I. K., Uhlmann, D. R. & Simonds, C. H. The thermal history of the Manicouagan Impact Melt Sheet, Quebec. *J. Geophys. Res. Solid Earth* **83**, 2789–2798 (1978).

39. Nagy, L. *et al.* Stability of equidimensional pseudo–single-domain magnetite over billion-year timescales. *Proc. Natl. Acad. Sci. U. S. A.* **114**, 10356–10360 (2017).

40. Gattacceca, J. *et al.* Paleomagnetism and rock magnetism of east and west clearwater lake impact structures. *Can. J. Earth Sci.* **56**, 983–993 (2019).

41. Behera, S. S., Tiwari, S., Pandey, A. K., Agarwal, A. & Ojha, A. K. The probable direction of impact at Dhala impact structure , India deciphered from microfracture intensity and X - ray diffractometry : a new potential impact direction indicator. *Earth, Planets Sp.* 1–11 (2024) doi:10.1186/s40623-024-02028-1.

42. Gattacceca, J., Lamali, A., Rochette, P., Boustie, M. & Berthe, L. The effects of explosive-driven shocks on the natural remanent magnetization and the magnetic properties of rocks. *Phys. Earth Planet. Inter.* **162**, 85–98 (2007).

43. Gattacceca, J. *et al.* Investigating impact demagnetization through laser impacts and SQUID

microscopy. *Geology* **34**, 333–336 (2006).

44. Roberts, A. P. *et al.* Resolving the Origin of Pseudo-Single Domain Magnetic Behavior. *J. Geophys. Res. Solid Earth* **122**, 9534–9558 (2017).

45. Bezaeva, N. S., Rochette, P., Gattacceca, J., Sadykov, R. A. & Trukhin, V. I. Pressure demagnetization of the Martian crust: Ground truth from SNC meteorites. *Geophys. Res. Lett.* **34**, 2–5 (2007).

46. Bezaeva, N. S., Gattacceca, J., Rochette, P., Sadykov, R. A. & Trukhin, V. I. Demagnetization of terrestrial and extraterrestrial rocks under hydrostatic pressure up to 1.2 GPa. *Phys. Earth Planet. Inter.* **179**, 7–20 (2010).

47. Gilder, S. A., Goff, M. Le & Chervin, J.-C. Static stress demagnetization of single and multidomain magnetite with implications for meteorite impacts. *High Press. Res.* **26**, 539–547 (2006).

48. Jackson, M., Borradaile, G., Hudleston, P. & Banerjee, S. Experimental deformation of synthetic magnetite-bearing calcite sandstones: effects on remanence, bulk magnetic properties, and magnetic anisotropy. *J. Geophys. Res.* **98**, 383–401 (1993).

49. Louzada, K. L., Stewart, S. T. & Weiss, B. P. Effect of shock on the magnetic properties of pyrrhotite, the Martian crust, and meteorites. *Geophys. Res. Lett.* **34**, 1–5 (2007).

50. Tikoo, S. M. *et al.* Preservation and detectability of shock-induced magnetization. *J. Geophys. Res. Planets* **120**, 1461–1475 (2015).

51. Nagata, T. & Carleton, B. J. Notes on Piezo-remanent Magnetization of Igneous Rocks. *J. Geomagn. Geoelectr.* **20**, 115–127 (1968).

52. Nagata, T. Basic magnetic properties of rocks under the effects of mechanical stresses. *Tectonophysics* **9**, 167–195 (1970).

53. Gilder, S. A., LeGoff, M., Chervin, J. C. & Peyronneau, J. Magnetic properties of single and multi-domain magnetite under pressures from 0 to 6 GPa. *Geophys. Res. Lett.* **31**, 1–5 (2004).

54. Nagata, T. Main Characteristics of Piezo-Magnetization and Their Qualitative Interpretation. *J. Geomagn. Geoelectr.* **18**, 81–97 (1966).

55. Pati, J. K. *et al.* Geochemical evidence of an extraterrestrial component in impact melt breccia from the Paleoproterozoic Dhala impact structure, India. *Meteorit. Planet. Sci.* **52**, 722–736 (2017).

56. Dunlop, D. J. & Özdemir, Ö. *Rock Magnetism: Fundamentals and Frontiers*. (Cambridge University Press, 1997).

57. Kuzina, D. M. *et al.* Paleomagnetic study of impactites from the Karla impact structure suggests protracted postimpact hydrothermalism. *Meteorit. Planet. Sci.* **57**, 1846–1860 (2022).

58. Mendes, B., Kontny, A., Dudzisz, K. & Wilke, F. Ries magnetic mineralogy: Exploring impact and post-impact evolution of crater magnetism. *Meteorit. Planet. Sci.* **59**, 1577–1609

(2024).

59. Kletetschka, G., Kavkova, R. & Ucar, H. Plasma shielding removes prior magnetization record from impacted rocks near Santa Fe, New Mexico. *Sci. Rep.* **11**, 1–13 (2021).

60. Carporzen, L., Gilder, S. A. & Hart, R. J. Palaeomagnetism of the Vredefort meteorite crater and implications for craters on Mars. *Nature* **435**, 198–201 (2005).

61. Narrett, I. S. *et al.* Impact plasma amplification of the ancient lunar dynamo. *Sci. Adv.* **11**, 1–11 (2025).

62. O'Keefe, J. D. & Ahrens, T. J. Impact-induced melting of planetary surfaces. in *Large Meteorite Impacts and Planetary Evolution* (eds. Dressier, B. O., Grieve, R. A. F. & Sharpton, V. L.) 0 (Geological Society of America, 1992). doi:10.1130/SPE293-p103.

63. Plescia, J. B. & Cintala, M. J. Impact melt in small lunar highland craters. *J. Geophys. Res. Planets* **117**, 1–12 (2012).

64. Dunlop, D. J. & Arkani-Hamed, J. Magnetic minerals in the Martian crust. *J. Geophys. Res. Planets* **110**, 1–11 (2005).

65. Rochette, P. *et al.* Matching Martian crustal magnetization and magnetic properties of Martian meteorites. *Meteorit. Planet. Sci.* **40**, 529–540 (2005).

66. Pati, Reimold, W. U., Koeberl, C. & Pati, P. *The Dhala Structure, Bundelkhand Craton, Central India-Eroded Remnant of a Large Paleoproterozoic Impact Structure*. *Meteoritics & Planetary Science* vol. 43 (2008).

67. Saha, L. *et al.* Crustal geodynamics from the Archaean Bundelkhand Craton, India: constraints from zircon U–Pb–Hf isotope studies. *Geol. Mag.* **153**, 179–192 (2016).

68. Pradhan, V. R., Meert, J. G., Pandit, M. K., Kamenov, G. & Mondal, M. E. A. Paleomagnetic and geochronological studies of the mafic dyke swarms of Bundelkhand craton, central India: Implications for the tectonic evolution and paleogeographic reconstructions. *Precambrian Res.* **198**–**199**, 51–76 (2012).

69. Deb, T. & Bhattacharyya, T. Earth-Science Reviews The evolution of the fracture systems under progressive sinistral shear in the Bundelkhand Craton , Central India : A review and new insights. *Earth-Science Rev.* **235**, 104238 (2022).

70. Singh, A. K. *et al.* Characteristic landforms and geomorphic features associated with impact structures: Observations at the Dhala structure, north-central India. *Earth Surf. Process. Landforms* **46**, 1482–1503 (2021).

71. Agarwal, A., Kumar, S., Joshi, G. & Agarwal, K. K. Evidence for shock provides insight into the formation of the central elevated area in the Dhala impact structure, India. *Meteorit. Planet. Sci.* **55**, 2772–2779 (2020).

72. Petrovský, E. & Kapička, A. On determination of the Curie point from thermomagnetic curves. *J. Geophys. Res. Solid Earth* **111**, B12S27 (2006).

73. Paterson, G. A., Zhao, X., Jackson, M. & Heslop, D. Measuring, Processing, and Analyzing Hysteresis Data. *Geochemistry, Geophys. Geosystems* **19**, 1925–1945 (2018).

74. Dunlop, D. J. Theory and application of the Day plot (Mrs/Ms versus Hcr/Hc) 1. Theoretical curves and tests using titanomagnetite data. *J. Geophys. Res. Solid Earth* **107**, EPM 4-1-EPM 4-22 (2002).

75. Dunlop, D. J. Theory and application of the Day plot (Mrs/Ms versus Hcr/Hc) 2. Application to data for rocks, sediments, and soils. *J. Geophys. Res. Solid Earth* **107**, EPM 5-1-EPM 5-15 (2002).

76. Lurcock, P. C. & Wilson, G. S. PuffinPlot: A versatile, user-friendly program for paleomagnetic analysis. *Geochemistry, Geophys. Geosystems* **13**, 1–6 (2012).

77. Fisher, R. A. Dispersion on a sphere. *Proc. R. Soc. London. A. Math. Phys. Sci.* **217**, 295–305 (1953).

78. Clark, D. A. & Emerson, J. B. Notes On Rock Magnetization Characteristics In Applied Geophysical Studies. *Explor. Geophys.* **22**, 547–555 (1991).

79. Pandey, A. K., Agarwal, A., Joshi, G., Sangode, S. J. & Venkateshwarlu, M. Data set of Shock demagnetization in an ambient magnetic field at the Dhala impact structure, India. (2025) doi:10.6084/m9.figshare.30851126.v3.

80. Jain, S. C., Gaur, V. P., Srivastava, S. K., Nambiar, K. V. & Saxena, H. P. Recent find of a cauldron structure in Bundelkhand Craton. *Geol. Surv. India Spec. Publ.* 289–297 (2001).

81. Day, R., Fuller, M. & Schmidt, V. A. Hysteresis properties of titanomagnetites: Grain-size and compositional dependence. *Phys. Earth Planet. Inter.* **13**, 260–267 (1977).

Acknowledgements

The SERB/ES/2020301 (DST, India), IITK/ES/2019372 (IIT Kanpur, India) and STC/ES/2025349 supported this study. AKP extends sincere gratitude to the Department of Science and Technology, New Delhi, Government of India, for their generous support in the form of an INSPIRE fellowship (IF190993). We thank the Department of Earth Sciences, Indian Institute of Technology Kanpur, for providing the optical microscopy and the working facilities.

Author contributions

A.K. Pandey: Conceptualization, fieldwork and sampling, sample analysis, data interpretation, writing original draft, review and editing. **A. Agarwal:** Conceptualization, data interpretation, review and editing, funding acquisition. **G. Joshi:** Fieldwork and sampling, review and editing. **S.J. Sangode:** Sample analysis, review and editing. **M. Venkateshwarlu:** Sample analysis, review and editing.

Competing interests

The authors declare no competing interests

Figure captions

Figure 1. Geological setting of the Dhala impact structure

Geological map of the Dhala impact structure, presenting major lithologies and sample locations. The map was prepared using ArcMap 10.7 and modified after [41,80]

Figure 2. Field photographs of major lithologies at the Dhala structure

(a) Impact melt rock with vesicles. (b) Monomict breccia composed of angular to sub-angular granitoid clasts embedded in a finer clastic matrix. (c) Outcrop of coarse-grained equigranular granite. (d) Medium-grained diorite displaying an interlocking texture of plagioclase and hornblende.

Figure 3. Petrographic characteristics of impactites and unshocked target rocks

(a) Quartz with Ballen structure in impact melt rock, (b) Planar deformation features embedded in impact melt rock. (c) Titanomagnetite (Ti-Mag) oxidized to titanohematite (Ti-Hem) along the margins in impact melt rock. (d) Monomict breccia with angular clasts of fractured granitoid embedded within a fine-grained matrix. (e) A clast of monomict breccia consisting of plagioclase (Plg) and quartz (Qtz) grains. (f) Unshocked granite with plagioclase (Plg) altered to sericite, quartz (Qtz), and biotite (Bio). (g) Unshocked diorite presenting interlocking texture of plagioclase (Plg) and hornblende (Hbl).

Figure 4. Thermomagnetic behaviour of the unshocked target and impact melt rock

Representative thermomagnetic curves showing variations in the magnetization with temperature for unshocked granite (a), unshocked diorite (b), and impact melt rock (c, d). The heating and cooling curves are shown in red and blue, respectively. T_{C1}, T_{C2}, T_{C3} and T_{C4} mark the Curie transition temperatures corresponding to Ti-poor magnetite, Ti-magnetite, pyrrhotite, and Ti-

hematite, respectively. See Supplementary Figs. 2 and 3 for thermomagnetic curves of other samples and Supplementary Table 3 for the values of each sample.

Figure 5. Magnetic hysteresis properties and domain-state classification

Representative hysteresis curves of the unshocked granite (a), unshocked diorite (b), and impact melt rock (c-d) showing variation in magnetization with applied field. (e) Day plot [74,75,81] showing the bulk domain behavior by plotting the ratio of remanent magnetization (M_{rs}), and saturation magnetization (M_s) against the ratio of remanence of coercivity (H_{cr}) and coercive force (H_c). The SD, MD, and PSD stand for single domain, multi-domain, and pseudo-single domain, respectively. The ratios for monomict breccia are taken from Tiwari et al. [14]. See Supplementary Table 2 for the values of each parameter and Supplementary Fig. 1 for the hysteresis curves of the rest of the samples.

Figure 6. Relationship between magnetic susceptibility and remanence properties

Plot showing the variation in Natural Remanent Magnetization (NRM) and Koenigsberger (Q) ratio with magnetic susceptibility. Cross symbols show mean values, and dashed ellipses represent two-dimensional 95% confidence ellipses based on the covariance of the log-transformed variables (green: unshocked granite and diorite; blue: monomict breccia; red: impact melt).

Figure 7. Alternating and thermal demagnetization behaviour

Demagnetization behaviour of representative samples is shown using Zijderveld diagrams and lower-hemisphere stereographic projections. (a–d) Alternating field (AF) demagnetization of unshocked target rocks (granite, UG, and diorite, UD). (e–f) AF demagnetization and (g–h) thermal demagnetization of monomict breccia samples. (i–j) AF demagnetization and (k–l) thermal demagnetization of impact melt rock samples. Solid and open symbols in the Zijderveld plots denote projections onto the horizontal and vertical planes, respectively. Stable components are shown in red. All plots were generated using PuffinPlot software v.1.4.1 [76]. Additional plots and data are provided in Supplementary Figures 6, 7, and 8 and Supplementary Tables 5 and 6.

Figure 8. Characteristic remanent magnetization directions

Equal-area lower-hemisphere stereographic projections of characteristic remanent magnetization (ChRM) directions for (a) unshocked target rocks and (b) impact melt rocks. Solid and open

symbols represent ChRM directions with positive and negative inclinations, respectively. Dashed/solid ellipses represent the α95 confidence limits for the mean ChRM. Mean directions were computed and plotted using PuffinPlot software v.1.4.1 [76]. Additional plots and data are provided in Supplementary Tables 5 and 6 and Supplementary Figs. 6 and 8.

Editorial summary:

Shock waves during impact events can significantly influence the magnetic properties of impact craters and their resulting paleomagnetic signatures, according to paleomagnetic measurements on a suite of samples from the Dhala impact structure

Peer review information:

Communications Earth and Environment thanks Banusha Kugabalan and the other, anonymous, reviewer(s) for their contribution to the peer review of this work. Primary Handling Editors: Claire Nichols and Joe Aslin. [A peer review file is available.

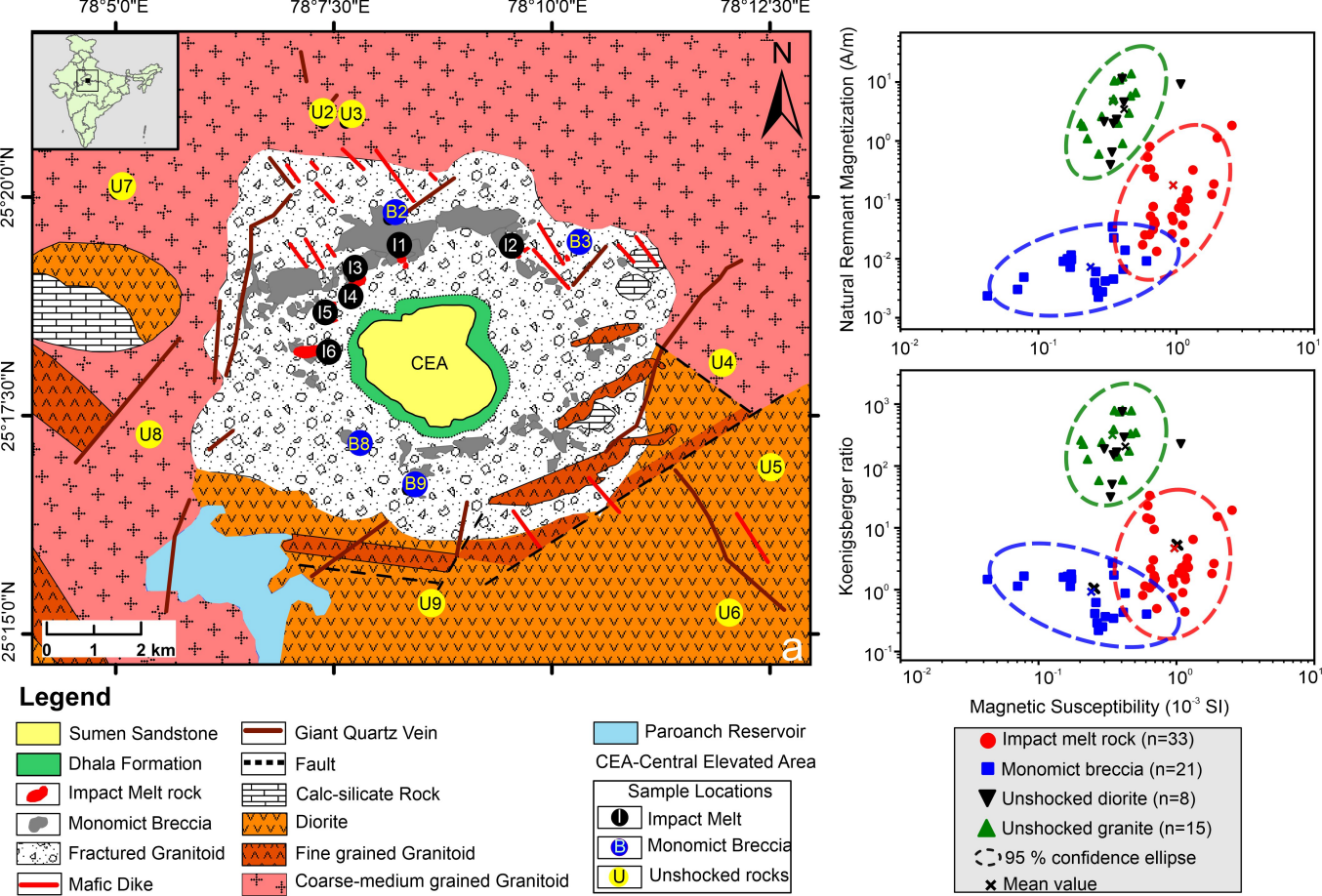
78°5'0"E
78°7'30"E
78°10'0"E
78°12'30"E
25°20'0"N
25°17'30"N
25°15'0"N
N
U2
U3
U7
B2
I1
I2
B3
I3
I4
I5
I6
CEA
U4
U8
B8
B9
U5
U9
U6
0 1 2 km
a
Natural Remnant Magnetization (A/m)
Koenigsberger ratio
Magnetic Susceptibility (10-3 SI)
Impact melt rock (n=33)
Monomict breccia (n=21)
Unshocked diorite (n=8)
Unshocked granite (n=15)
95 % confidence ellipse
Mean value
Legend
Sumen Sandstone
Dhala Formation
Impact Melt rock
Monomict Breccia
Fractured Granitoid
Mafic Dike
Giant Quartz Vein
Fault
Calc-silicate Rock
Diorite
Fine grained Granitoid
Coarse-medium grained Granitoid
Paroanch Reservoir
CEA-Central Elevated Area
Sample Locations
Impact Melt
Monomict Breccia
Unshocked rocks

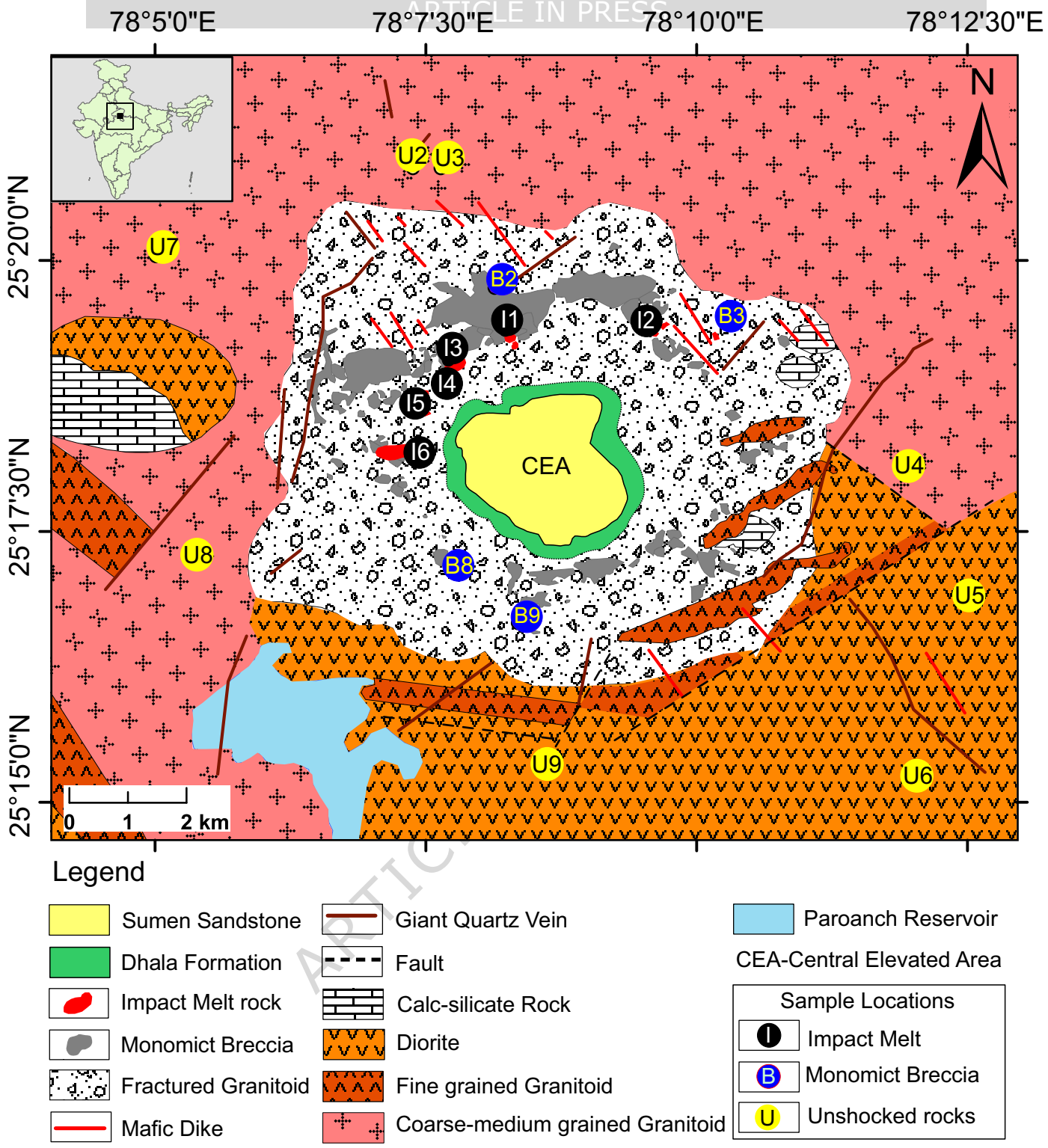

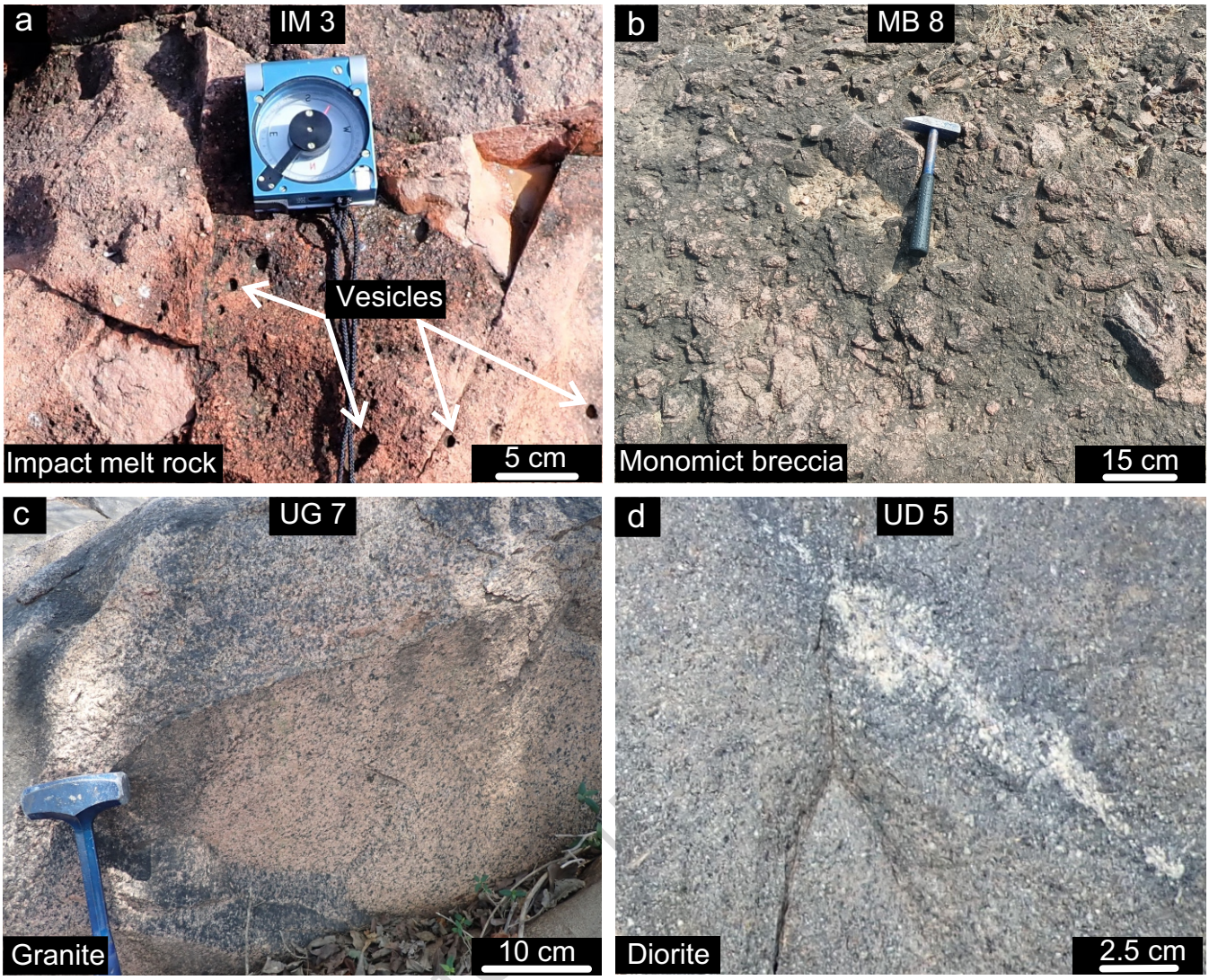

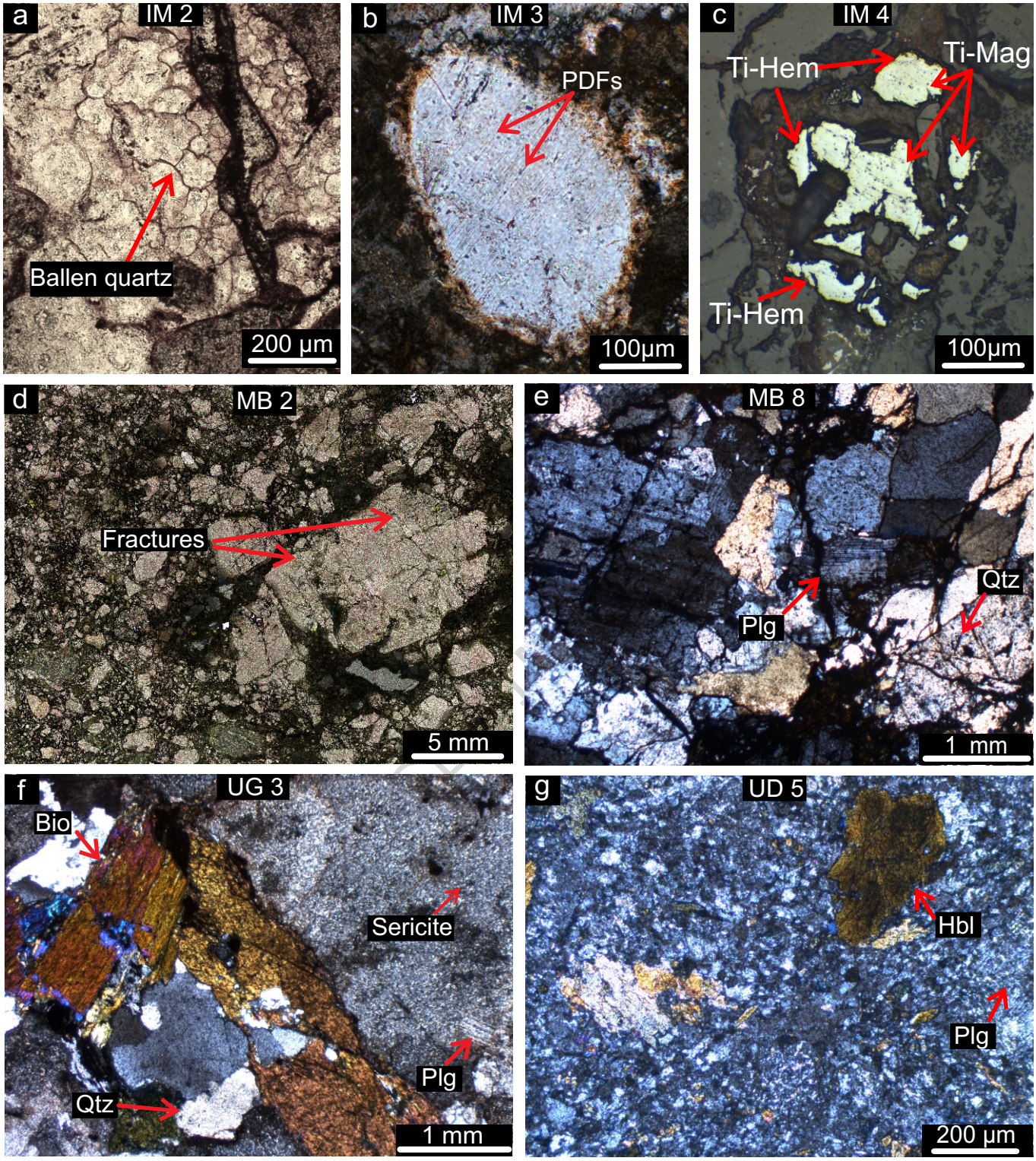
a
IM 2
Ballen quartz
200 µm
b
IM 3
PDFs
100µm
c
IM 4
Ti-Hem
Ti-Mag
Ti-Hem
100µm
d
MB 2
Fractures
5 mm
e
MB 8
Plg
Qtz
1 mm
f
UG 3
Bio
Sericite
Plg
Qtz
1 mm
g
UD 5
Hbl
Plg
200 µm